Electrochemical Impedance Characterization of LiMnPO₄ Electrodes with Different Additions of MWCNTs in an Aqueous Electrolyte

Jesus Israel Barraza-Fierro[1], Tse-Ming Chiu[1], and Homero Castaneda[1*]

[1]Department of Materials Science and Engineering, University of Texas A&M, College Station, TX, USA.

Corresponding author: Homero Castaneda, e-mail: hcastaneda@tamu.edu , Phone: +1 (979) 458 9844

Abstract. An electrochemical characterization was performed in electrodes with different weight percentages of LiMnPO₄ and multi-walled carbon nanotubes (MWCNTs) in aqueous solution. The redox potential of LiMnPO₄ cathode is close to the electrolyte decomposition, which provides an ideal scenario to study multiple reactions on a single electrode surface involving parallel steps and species transformation in both solid and liquid state. Different processes were deconvoluted using cyclic voltammetry and electrochemical impedance spectroscopy. In addition, a surface coverage model was employed to theoretically quantify the limiting step of the electrochemical process. The results show the addition of MWCNTs increased the electrical conductivity of the cathode and improved the intercalation process in LiMnPO₄. The optimal concentrations of MWCNTs, which enhanced the electrical properties and decreased the water oxidation effect, were 20 and 40 wt.%.
Keywords: electrochemical impedance spectroscopy; coverage model; aqueous rechargeable lithium battery; lithium magnesium phosphate; lithium intercalation; oxygen evolution reaction.

Resumen. Una caracterización electroquímica fue llevada a cabo en electrodos con diferentes porcentajes en peso de LiMnPO₄ y nanotubos de carbón de pared múltiple (MWCNTs por sus siglas en inglés) en solución acuosa. El valor de potencial de desintercalación de LiMnPO₄ está cercano a aquel de descomposición del agua, lo cual produce un escenario ideal para estudiar reacciones múltiples en una sola superficie que involucra procesos paralelos y transformación de especies en estado sólido y líquido. Varios procesos fueron deconvolucionados en dichos materiales usando voltametría cíclica y espectroscopia de impedancia electroquímica (EIS por sus siglas en inglés). Para analizar los datos de EIS, un modelo de cobertura fue empleado para cuantificar teóricamente el paso limitante del proceso electroquímico. Se obtuvo que la adición de MWCNTs incrementó la conductividad eléctrica del cátodo y mejoró el proceso de intercalación en el LiMnPO₄. Las concentraciones óptimas de MWCNTs para aumentar las propiedades eléctricas y disminuir el efecto de oxidación del agua fueron 20 y 40% en peso.
Palabras clave: espectroscopia de impedancia electroquímica; modelo de cobertura; baterías recargables de litio acuosas; fosfato de litio y manganeso; intercalación de litio; reacción de evolución de oxígeno.

Introduction

Batteries used in large-scale applications should have a low cost, a good safety, a long cycle-life, a high power deliverance, and a good charging rate [1]. Organic type lithium-ion batteries (LIB) may be an excellent candidate for such applications due to their high energy density (> 120 Wh Kg^{-1}), but they suffer from severe safety and economic problems in terms of large scale application [2]. These batteries contain flammable organic electrolytes, which tend to ignite, to cause explosions, and to produce smoke in wrong operating conditions [3]. Furthermore, they are expensive due to their water sensitive assembly environment and the use of costly organic salts and electrolytes [4].

This situation has prompted the developed of less-expensive "green" battery materials and devices using aqueous electrolytes [4-6]. However, there are challenges adopting aqueous electrolytes (e.g., a smaller electroactive zone, material degradation in the presence of oxygen, co-intercalation of the proton, the side reaction of hydrogen-oxygen evolution, and the dissolution of the electrode materials) [7, 8]. Although these challenges are difficult, aqueous electrolyte batteries are promising to use in large-scale applications. Research has been conducted in neutral and alkaline solutions using $LiCoO_2$, $LiMn_2O_4$, $LiNi_xCo_{1-x}O_2$, and $LiFePO_4$ as cathodes [2, 9-11]. Among these materials, olivine-type $LiMPO_4$ cathodes (where M=Co, Fe, Mn, or Ni) have emerged as a promising alternative [12-14]. For example, the $LiMnPO_4$ compound is low cost, non-toxic, and easy to fabricate [15, 16]. However, pure $LiMnPO_4$ has an intrinsic low electronic conductivity [17]. This feature could be increased by adding conductive carbon (15–30%) [18, 19], but carbon has to be limited because it can increase the electrode surface area and enhance the kinetics of water oxidation [20].

The electrochemical response of LIB has to be studied using different electrochemical techniques such as cyclic voltammetry (CV) and electrochemical impedance spectroscopy (EIS) [21-24]. EIS is a powerful tool for distinguishing and evaluating electrochemical mechanisms. However, interpreting the results can be difficult [25]. Hence, different strategies have been implemented such as simple equivalent circuits, transmission line modeling, mechanistic models, reaction mechanisms, and neuronal networks [25-28].

The most common method that is used for describing EIS results is electric analogs. However, this type of analysis is incomplete because it can only reproduce certain electrochemical properties due to the lack of electrical elements associated with the process in electrochemical reactions such as diffusion, adsorption/desorption, and the negative impedance of depassivation processes [29]. Hence, other interpretation methods are required to describe EIS results. The coverage model developed by Epelboin [30] describes the reaction of adsorbed species and their electrochemical behavior on an electrode surface. This model uses a small sine wave perturbation of potential to quantify the electrochemical reaction constants, the coverage factor of one or more intermediates adsorbed at the interface, and the double layer capacitance. The model has been adapted to intercalation cathodes [21] and to growing of lithium dendrites [31].

This work aims to characterize the electrochemical behavior of $LiMnPO_4$ cathodes with the addition of multi-walled carbon nanotubes (MWCNTs) to improve their electronic conductivity. Cyclic voltammetry was used to identify the potential of reactions, the capacitive behavior of the composite, and the faradaic components. In addition, EIS was applied to identify and quantify the mechanism at the interface using an adaptation of the coverage model to analyze the results.

Experimental

$LiMnPO_4$ preparation and characterization

The precursor solution was made up of $LiNO_3$ (reagent grade; Sigma Aldrich, 3.48g), $Mn(NO_3)_2 \cdot 4H_2O$ (ACROSS; 97.5%, 12.94g), H_3PO_4 (Sigma Aldrich; 85 wt.%, 12.94g), and citric acid (Sigma Aldrich; 99%, 19.2g). These compounds were dissolved in a mixture of ethanol (20g) and water (40g). The solution was heated to 80°C for 12h on a hot plate and then dried at 120°C in a vacuum oven. Subsequently, the powder was stored at 550°C for 10h, mixed, and ground. Finally, the sample was heated at 700°C in air for 10h. The crystal structure of $LiMnPO_4$ was characterized using a Bruker D8 diffractometer with a Cu target operating at 40kV-40mA.

Electrode preparation and characterization

LiMnPO$_4$ and MWCNTs (Aldrich 724769 O.D.×L. 6–9nm×5μm, 95% carbon) were mixed in different quantities to achieve 90wt% of the cathode weight, and the other 10wt% was a binder of polyvinylidene fluoride (PVDF, Kynar HSV-900). The solvent was 1-methyl2-pyrrolidine (NMP, ACROSS), and the number of milliliters added to the composite varied for each composition. The mixture was placed on a 316 stainless steel current collector and dried at 120°C for 12h. The slurry thickness was leveled at 30μm using a doctor's blade. Table 1 lists the LiMnPO$_4$ and MWCNTs ratios existing in 90wt% of the cathodes. A Tescan LYRA-3 GMH, scanning electron microscopy (SEM), was used to obtain high-resolution images of the active material geometry. The porosity was determined using optical microscopy and SEM. The images were processed using Image Processing and Analysis in Java (Image J) to obtain the pore number, diameters, areas, and porosity [32].

Electrochemical characterization

The electrochemical experimentation was carried out in a three-electrode arrangement. The working electrode was the composite mixture placed on a current collector (316 stainless steel), the reference electrode was Ag/AgCl (KCl saturated), and the counter-electrode was a Pt mesh. The area of the working electrode was 11.40 cm^2 with loading of approximately 9 mg. The electrolyte was made up of 1M LiNO$_3$/ HNO$_3$ with a pH=2.

Cyclic voltammetry was set at a scan rate of 0.5 mV s^{-1} toward the positive scan direction with lower and upper boundaries of 0.4 and 1.4V vs. Ag/AgCl, respectively. The positive scan direction is set to promote the delithination reaction at the first battery cycle. The third cycle was reported in Fig. 3 to represent the redox potential in the followed charge-discharge condition. Electrochemical impedance spectroscopy was performed in a frequency range of 0.1–10000 Hz with 5mV of applied amplitude. The experiments were conducted using a Bio-logic SP-200^{TM}. Different bias potentials were applied: 0.8, 1.0, 1.2, and 1.4 V vs. Ag/AgCl.

Table 1. Composition ratio of each cathode for the 90wt% of the real weight and porosity of each electrode.

Cathode	Ratio (LiMnPO$_4$/MWCNT)	% Porosity
1	0/100	17.29
2	20/80	17.99
3	40/60	15.91
4	60/40	16.57
5	80/20	13.49
6	100/00	15.59

Coverage factor model adapted to the intercalation of lithium

The intercalation reaction of the LiMnPO$_4$ cathode is shown by the following equation (1):

$$LiMnPO_4 \underset{k_2}{\overset{k_1}{\rightleftharpoons}} Li_{1-x}MnPO_4 + xLi^+ + xe^- \tag{1}$$

where, k_1 is the oxidation reaction constant: $k_1 = k_1^0 \exp(aE)$, k_1^0 is the standard oxidation constant, a is the kinetic parameter for the oxidation process, E is an arbitrary potential, k_2 is the reduction constant: $k_2 = k_2^0 \exp(-bE)$, k_2^0 is the standard reduction constant, and b is the kinetic parameter for the cathodic process.

The charge balance is given by equation (2):

$$i_F = nF\left[k_1\theta - k_2\left[\frac{Li^+}{Li^0}\right](1-\theta)\right] \tag{2}$$

where, F is the Faraday constant=96500 C/eq, n is the number of equivalents per mole, θ is the fraction of the total surface occupied by the intercalation of lithium, Li^0 is the lithium ion concentration of a standard state, and Li^+ is the lithium ion concentration near the interface after polarization [33].

The faradaic current density (i_F) for a small sine wave perturbation of potential is given by equation (3):

$$\delta i_F = \left(\frac{\partial i_F}{\partial E}\right)\delta E + \left(\frac{\partial i_F}{\partial \theta}\right)\delta\theta \tag{3}$$

Hence, the faradaic admittance due to this perturbation is obtained via the dependence of current on voltage, as shown in equation (4)

$$Y_F = \frac{\delta i_F}{\delta E} = \left(\frac{\partial i_F}{\partial E}\right) + \left(\frac{\partial i_F}{\partial \theta}\right)\left(\frac{\delta\theta}{\delta E}\right) \tag{4}$$

The partial derivatives of current with respect to potential and intercalation fraction are shown in equation (5) and (6), respectively.

$$\frac{\partial i_F}{\partial E} = F\left[ak_1\theta + bk_2\frac{[Li^+]}{[Li^0]}(1-\theta)\right] \tag{5}$$

$$\frac{\partial i_F}{\partial \theta} = F\left[k_1 + k_2\frac{[Li^+]}{[Li^0]}\right] \tag{6}$$

The relation of intercalation fraction and the potential can be obtained from the equation (2). However, the dependence of the intercalation fraction as a function of time in non-steady conditions has to be used in the mathematical formulation and it is shown in the following expression [21, 26, 30].

$$\beta \frac{d\theta}{dt} = i_F = F\left[k_1\theta - k_2 \frac{\left[Li^+\right]}{\left[Li^0\right]}(1-\theta) \right] \tag{7}$$

Linearizing the expression (7) for a small wave perturbation, the equation (8) is acquired [21, 26, 30].

$$\beta j\omega\delta\theta = F\left[\left[ak_1\theta + bk_2 \frac{\left[Li^+\right]}{\left[Li^0\right]}(1-\theta) \right]\delta E + \left[k_1 + k_2 \frac{\left[Li^+\right]}{\left[Li^0\right]}(1-\theta) \right]\delta\theta \right] \tag{8}$$

Here, β is the charge density for a monolayer of adsorbed species and ω is the angular frequency.

This expression can be rearranged to obtain the last term of equation (4), which is shown below as equation (9).

$$\frac{\delta\theta}{\delta E} = F\left[\frac{ak_1\theta + bk_2 \frac{\left[Li^+\right]}{\left[Li^0\right]}(1-\theta)}{\beta j\omega - F\left[k_1 + k_2 \frac{\left[Li^+\right]}{\left[Li^0\right]} \right]} \right] \tag{9}$$

Including equations (5), (6), and (9) in equation (4), the faradaic admittance (Y_F) is completed. In addition, mass transport has to be evaluated because it is an important phenomenon in the intercalation process. The expression for Warburg diffusion was applied and is presented in equation (10).

$$Z_w = \sigma\omega^{-1/2} - \sigma j\omega^{-1/2} \tag{10}$$

where, σ is the Warburg coefficient for diffusion based on the solution of a semi-infinite solid [21].

The faradaic admittance (Y_F), equation (4), the Warburg impedance (Z_w), and the double layer capacitance (Q_{dl}) can be combined to acquire the total electrochemical impedance (Z_t), as shown in equation (11).

$$Z_t = \frac{1}{\dfrac{1}{\dfrac{1}{Y_F} + Z_w} + Q_{dl}\left(j\omega\right)^{n_{dl}}} \tag{11}$$

The impedance of the Li deintercalation process on a porous electrode was described by Levi et al. [34]. They noted that the EIS response of the composite by itself has to be evaluated in addition to the electrochemical effect because the microstructure influence of the porous film and the electrolyte (R_e) were acquired between 1 and 10^4 Hz. Therefore, the total impedance of the interface is shown in equation (12).

$$Z_{ts} = R_e + \left(\frac{1}{\frac{1}{R_{film}} + Q_{film}\left(j\omega\right)^{n_{film}}} \right) + Z_t \tag{12}$$

Electric analog for water oxidation reaction at a porous electrode

The equivalent analog that represents electrochemical reactions (e.g., water oxidation) at a porous interface is a parallel combination of the reaction resistance and the capacitance of the double layer [35]. This last element combination is in series with the film resistance, and all of these components are in parallel with the film capacitance [35]. The mathematical expression is shown in equation (13).

$$Z_{t2} = R_e + \frac{1}{\frac{1}{R_{film} + \frac{1}{\frac{1}{R_{ct}} + Q_{dl}(j\omega)^{ndl}}} + Q_{film}\left(j\omega\right)^{n_{film}}} \tag{13}$$

where, R_e is the electrolyte resistance, R_{ct} is the charge transfer resistance for the water oxidation, Q_{dl} is the pseudocapacitance for the water oxidation species, and n_{dl} is the exponent of the constant phase element (CPE).

Z_{t2} is the impedance of all the cathodes at 1.4V. In addition, this model was applied to cathode 1 (0% $LiMnPO_4$) due to the lack of $LiMnPO_4$ at all potentials, and to find the response of electrode 6 (100% $LiMnPO_4$) resulted from the low electric conductivity at all the potentials.

Results and discussion

X-ray diffraction results

The powder diffraction pattern of the synthesized $LiMnPO_4$ is shown in Fig. 1. The Bragg peaks of the processed compound matched the standard pattern of $LiMnPO_4$ (JCPDS# 33−0803) with a narrow peak width intensity, which can be classified as a highly crystalloid, single-phase, olivine-type $LiMnPO_4$.
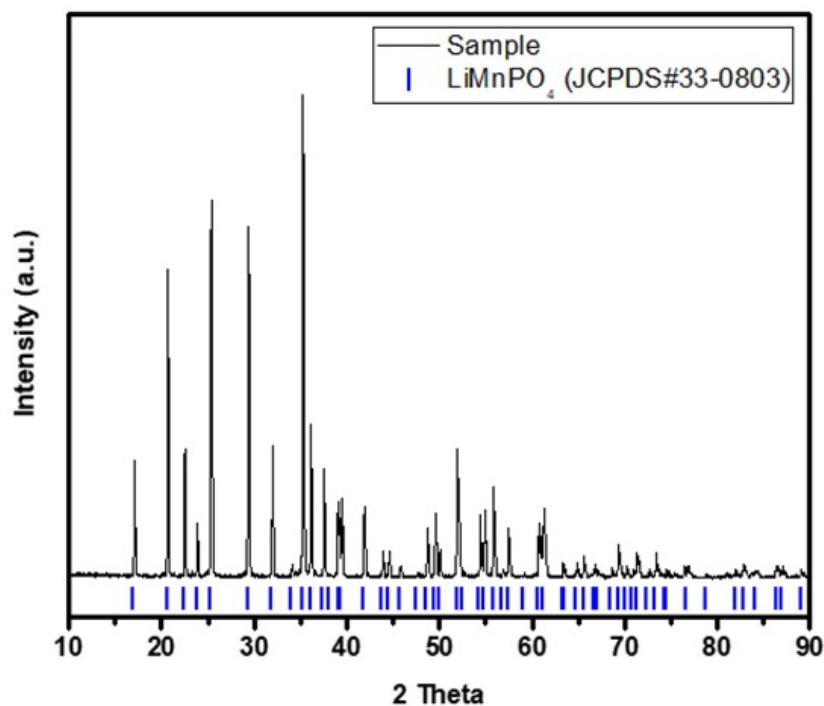
Fig. 1. X-ray diffraction pattern of the synthesized LiMnPO$_4$

Scanning electron microscope results

The scanning electron microscope images are shown in Fig. 2. For cathode 1 (0% LiMnPO$_4$), the MWCNTs were intertwined into a spindle-like microstructure with a hierarchical distribution of pore size. The PVDF dissolved in NMP has been characterized previously [36]; it exhibited a porous morphology as the one acquired in this study. The percentage of porosity is uniform for all the electrodes, as shown in Table 1. This fact ensures that the liquid phase transportation property persists from cathode 1 to 6. For cathode 2 (20wt% LiMnPO$_4$), there were white spots that revealed LiMnPO$_4$ has a low electrical conductivity, and a charging effect is acquired. For electrode 3 (40wt% LiMnPO$_4$), the particles were distributed in the MWCNT networks with increase in surface density. For cathode 4 (60 wt%LiMnPO$_4$), the surface density of LiMnPO$_4$ can be found significantly increased and some aggregates of sizes around $10-15$ um can be observed. For cathode 5 (80wt% LiMnPO$_4$), there was a wider distribution of particles. However, the fraction of areas with aggregates increased significantly compared with the other cathodes. Cathode 6 (100wt.% LiMnPO$_4$) was completely occupied by LiMnPO$_4$ based on the white color due to the charging of LiMnPO$_4$.
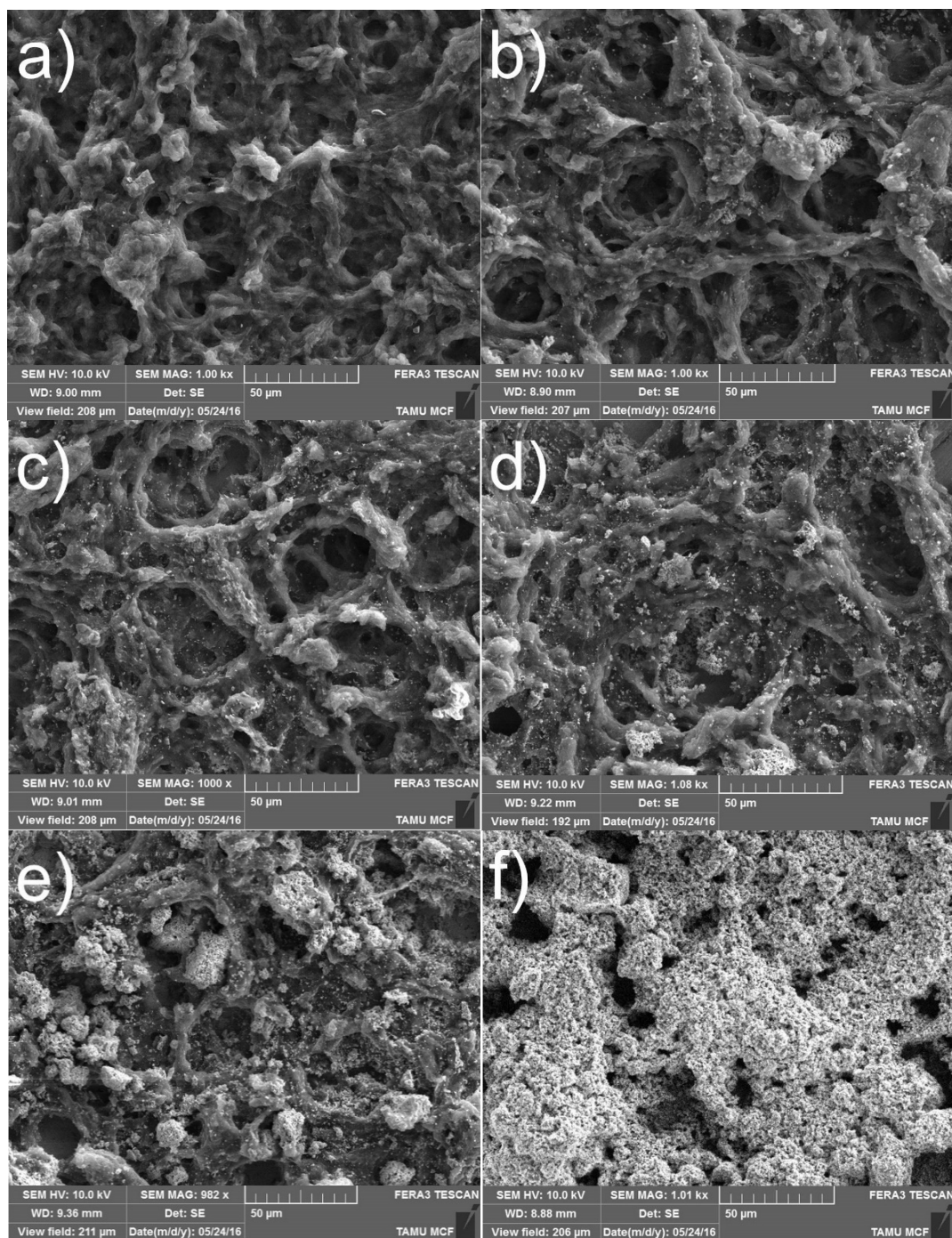
Fig. 2. Scanning electron microscopy image of the active material with different LiMnPO$_4$ percentages (**a**) 0, (**b**) 20, (**c**) 40, (**d**) 60, (**e**) 80, and (**f**) 100 wt%.

Voltammetry

The goal of this electrochemical test was to determine the reaction potentials in the system. As a result, the scanning window was established in the range from -500mV to + 500mv in relation to 0.9V vs. Ag/AgCl [37-39]. There are several phenomena that can be obtained in the CVs of Li_xMnPO_4/MWCNTs electrodes such as the capacitance of the composite material, the intercalation-deintercalation of Li^+ from the $MnPO_4$ host, and the water oxidation when the potential swift was higher than the operation window offered by the electrolyte.

The CV results for cathode 1 are shown in Fig. 3**(a)**. A flat response of the current is obtained from 0.5–1.1 V. The current increases its value from 1.1 V to 1.4 V. Any reduction current can be observed in the backward scan from 1.4 to 1.1V until a plateau was obtained again from 1.0–0.4 V. This result is associated with a capacitive behavior and a non-reversible electrochemical reaction. The former is related to the capacitive behavior of the electrode composite by itself, and the latter is related to the oxidation of water.

The results of cathodes 2 and 3 (20 and 40wt% $LiMnPO_4$) are shown in Fig. 1**(a)**. For both electrodes, the current is constant from 0.5–1.1 V, and then it increases with a maximum around 1.2 V. Subsequently, a peak is obtained at 1.4 V (the vertex potential) where the current is 5.3 and 3.9 mA for electrodes 2 and 3, respectively. In the reverse scan, a cathodic peak was obtained at 1.0 V for electrode 2 and 0.9 V for electrode 3. At potentials lower than 0.8 V but above 0.4 V, the current exhibited a flat behavior. These results can be linked to the capacitive behavior of the composite, one pseudo-reversible electrochemical reaction associated with the intercalation of lithium, and one non-reversible reaction related to the oxidation of water.

The behaviors of cathodes 4 and 5 (60 and 80wt% $LiMnPO_4$) are shown in Fig. 3**(b)**. There is a capacitive behavior that is not completely square due to a pseudo-reversible electrochemical reaction (deintercalation) and the overlap with the electrochemical irreversible process (water oxidation). The difference between the anodic and cathodic peaks for the pseudo-reversible reaction is higher than the one for electrodes 2 and 3. The increment in the current response is related to the larger quantity of $LiMnPO_4$. The maximum current at 1.4 V was 3.3 mA for electrode 4 and 2.6 mA for electrode 5. These results reveal that the capacitive double layer composite response is less important and that the pseudo-reversible reaction is the primary process for storing energy in this potential region. The oxidation of water was noted as well, but the kinetics of the process decreased based on the current magnitudes in the pure water oxidation behavior. The vertex potential was adopted as an example.

The results of cathode 6 (100 wt% $LiMnPO_4$) are shown in the zoom-in of Fig. 3**(b)**. The graph has a square behavior between 0.4–1.0 V for currents around 0.05 mA, and then it behaved like electrode 1 at the higher potential region. However, the maximum current was 0.1 mA at 1.4 V. In the reverse scan, the current followed the same line as the oxidation of water until a current plateau was attained from 0.4–1.3 V. This behavior is associated with the capacitance of the $LiMnPO_4$/binder and the water oxidation.
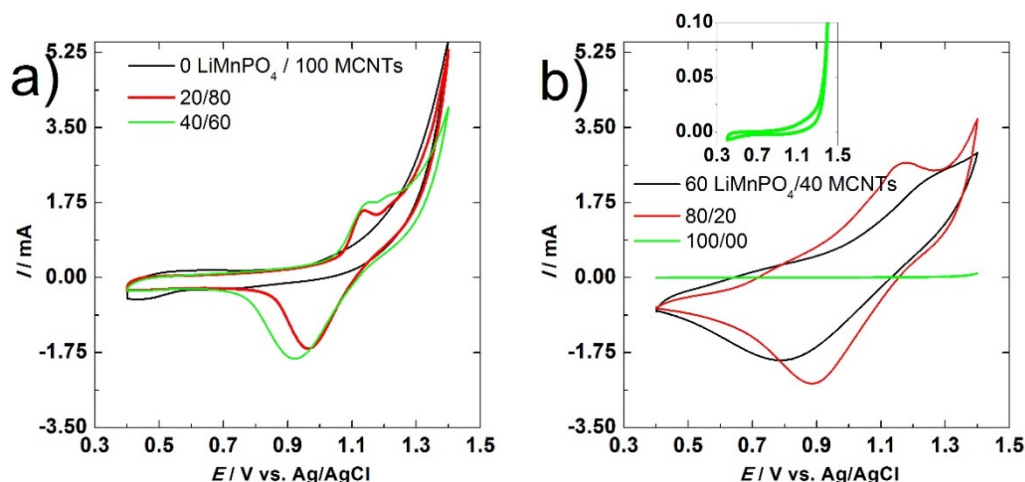

Fig. 3. (a) Voltammetry results for electrode 1, 2 and 3, and **(b)** for electrodes 4, 5 and 6, including a zoom for electrode 6.

Electrochemical impedance spectroscopy

The lithium intercalation process in organic electrolytes has been studied previously using EIS [34, 40, 41]. These studies have shown that a semicircle obtained at high frequency (HF) should be associated with the formation of a surface electrolyte interface (SEI), which in turn involves the migration effect into this layer. Furthermore, a semicircle at medium frequency (MF) should be related to the intercalation kinetics, a line with a slope around 45° in the Nyquist representation is due the solid diffusion in the composite particles and/or the diffusion in the electrolyte at low frequency (LF) [42], and a pure capacitive result at LF is linked to the charge storage of battery materials [40]. In addition, the semicircle at HF is due to the roughness of current collector and the porosity of a thick composite coating [33].

In the case of an aqueous electrolyte (e.g., $LiNO_3/HNO_3$), SEI formation might be absent or its effect could be negligible due to an ultra-thin film produced in highly conductive electrolytes [43]. However, other studies have proposed a SEI formation in an aqueous solution based on the surface layer model [43, 44]. In this work, the response of a semicircle at HF is not associated with a SEI because its presence has been acquired at a high solute concentration (e.g., 5 M $LiNO_3$) [43]. The impedance of the current collector in 1M $LiNO_3$ was tested and the EIS magnitudes were on the order of 10^5 Ω cm^2 and adsorption was acquired at 1.2 and 1.4 V of bias potential. Those features were not noted when the composite was on the current collector. Therefore, the current collector response is not linked to the results at HF. Hence, we included a circuit analog that was made of a parallel combination of R_{film} and Q_{film}, as shown in equation (12) connected in series with equation (11) associated at HF as the composite response.

The results of cathodes 1, 2, and 3 (ranging from 0–40wt% $LiMnPO_4$) are shown in Fig. **4(a–c)**. There is a dispersed semicircle at HF-MF and a capacitive line at LF. The dispersed semicircle is slightly dependent on the bias potential, and the capacitive behavior strongly changes with the bias perturbation. The former has a very small increment/decrement in its diameter, and the latter diminishes from a capacitive line at 0.8 V to another semicircle at 1.4 V. The semicircle at HF-MF is the physical response of the composite layer and the charge transfer reaction of $LiMnPO_4$, and its change is due to the applied bias potential on the $LiMnPO_4$ material. On the other hand, the semicircle at LF has a slope over 45°. The high capacitive behavior is resulted from water adsorption on the MWCNTs for electrode 1 and adsorption of water-deintercalation of lithium for electrodes 2 and 3. The semicircle at LF and 1.4 V is completely linked to water oxidation reaction as it was observed in the CV results.

The Nyquist diagrams for electrodes 4 and 5 (60 and 80%$LiMnPO_4$) are illustrated in Fig. **4(d–e)**. These electrodes show different behavior. A semicircle is recorded at HF and MF, and a line with a slope around 45° is obtained at LF. The semicircle at HM-MF decreased in diameter as the potential increased; the line at LF remained the same magnitude up to 1.4 V, where its shape changed to another semicircle. The semicircle is now attributed to the delithination reaction, and its diameter change is due to the potential modification that results in an increase in the reaction rate. At LF, the line results from the Li^+ solid-state diffusion in the $LiMnPO_4$. At 1.4 V, the semicircle at HF is associated with the layer, and the one at LF purely results from the water oxidation process inside the pores.

The impedance behavior of electrode 6 is shown in Fig. 5. It seems that only a partial-semicircle is acquired in the Nyquist diagram **(**Fig. 5 **(a))** at potentials below 1.1V. At 1.4 V, the clear semicircle is completely distinguishable. However, the Bode phase angle diagram that is shown in Fig. 5 (**b**) clarifies there are two overlapped processes. They decrease their maximum phase angle with the potential increment. This behavior corresponds to an electrochemical reaction at porous surfaces. The first maximum is associated with the composite material, and the second is associated with the oxidation of water. This idea is supported by the CV results for electrode 6. There was not a lithium reaction due to the extremely low conductivity of $LiMnPO_4$.
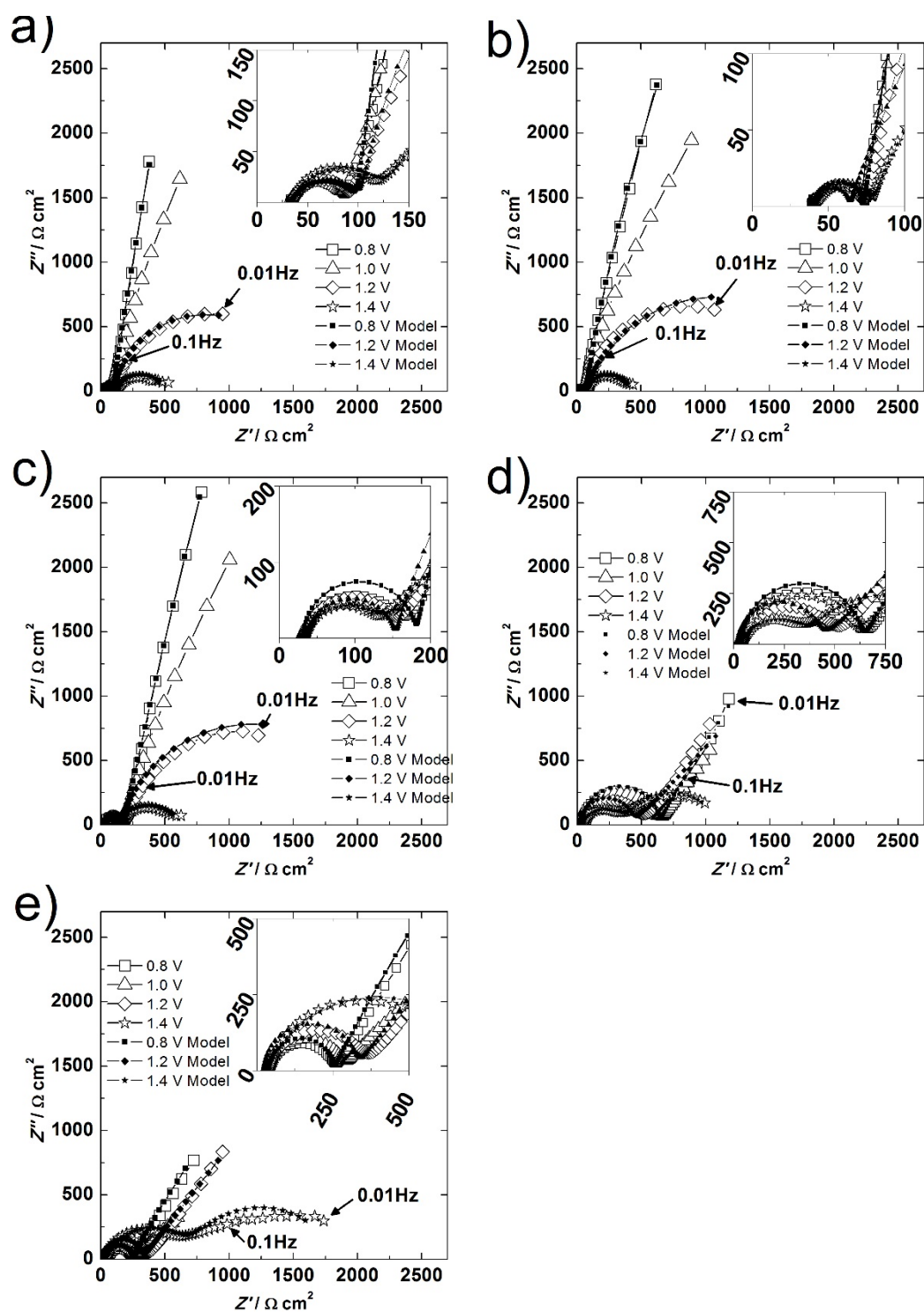
Fig. 4. Nyquist diagrams at different bias potentials (vs. Ag/AgCl) for Cathode 1 **(a)**, Cathode 2 **(b)**, Cathode 3 **(c)**, Cathode 4 **(d)**, and Cathode 5 **(e)**.
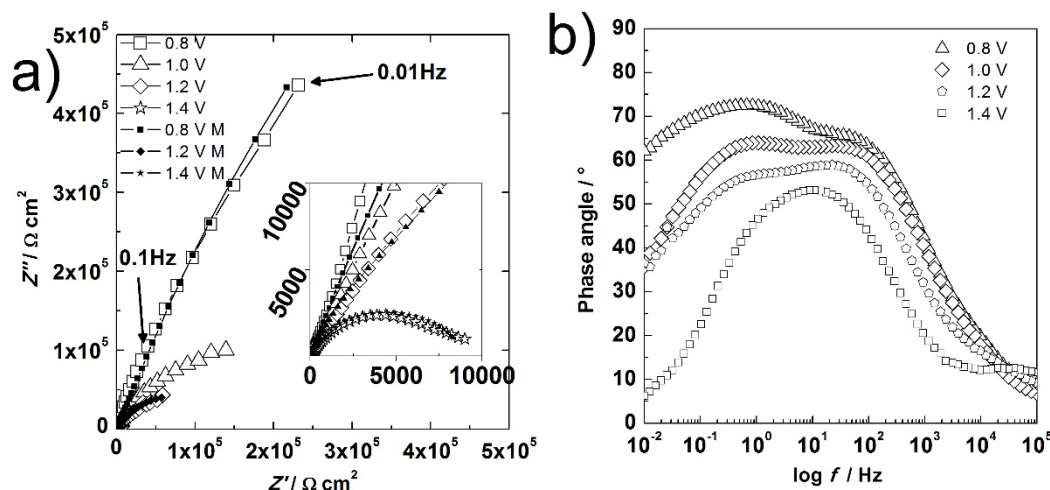
Fig. 5. Nyquist and Bode diagrams at different bias potentials (vs. Ag/AgCl) for electrode 6.

Quantitative results of EIS

The variables were quantified by fitting the experimental results to the proposed model. The fitting process follows five steps that have been described previously and involve applying genetic algorithms, evolution strategies, and the Levenberg-Marquardt method [45]. The solutions have to be found among meaningful physical ranges of the variables. The results of the fittings are shown in figures 4–5, where good agreement can be observed.

The experimental results were fitted at 0.8, 1.2, and 1.4 V because they showed three different situations of the system. At 0.8 V, the main effect should be the capacitive behavior of the composite film with little intercalation current. At 1.2 V, the response should be mainly due to the deintercalation reaction of Li, but the water oxidation effect was recorded as well. At 1.4 V, the water oxidation is associated with the results. All the fitted parameters are listed in Tables 2–4.

The values of the reaction constants are related to the charge transfer resistance (R_{ct}) and overpotential (E). If the values of the reaction constants decrease, R_{ct} will increase. This observation is in agreement with our results. R_{ct} is higher at 0.8 V than at 1.2 V or 1.4 V, which is consistent with the electrochemical reaction constants for Li deintercalation. The constants are around $10^{-5} \cdot 10^{-6}$ mol cm^{-2} s^{-1}for all the electrodes at 0.8 V [31], and they are around 10^{-2} mol cm^{-2} s^{-1} at 1.2 V [31].

Another important phenomenon is the diffusion of Li, which is linked to The Warburg coefficient (σ). The presence of σ indicates that solid state diffusion and the electrochemical reaction are controlling the system in a so-called "mixed-control mechanism." The diffusion process was completely acquired in the electrode with 60 and 80wt% LiMnPO$_4$. The values reveal the diffusion rate in the sample with 80%LiMnPO$_4$ was higher than in the one with 60%LiMnPO$_4$. The higher rate of diffusion observed in cathode 5 (80%) compared with cathode 4 (60%) at 0.8 V can be explained by the rate of the electrochemical reaction and film composition. As the concentration of MWCNTs increases, the solid diffusion of lithium is facilitated because more current is crossing the LiMnPO$_4$ particles and the deintercalation reaction is improved. This means the concentration difference (driving force) between the surface and center of the particles is higher in electrode 4 than in electrode 5. However, the semicircle at HF and MF has a diameter of 500–750 Ω cm^2 for electrode 4 and 250–300 Ω cm^2 for electrode 5. R_{ct} could apparently be higher due to the presence of adsorbed species on the MWCNTs that increase the electrochemical resistance. The same diffusion behavior and explanation are valid at 1.2 V, but the values of the Warburg coefficient, σ, are much lower because the concentration gradient is much higher. This is due to an increase in the electrochemical reaction rate and migration is more important inside the pores.

Table 2. Fitting results of the proposed model at 0.8V of bias potential.

Electrode /Variable	R_{film} (Ω cm²)	Q_{film} (F cm⁻² s¹⁻ⁿ)	n_{film}	R_{ct} (Ω cm²)	Q_{dl} (F cm⁻² s¹⁻ⁿ)	n_{dl}	R_e (Ω cm²)	-	-	-	-	-	-	-
1	66.96	1.27×10^{-4}	0.7	98972	6.85×10^{-3}	0.91	32.92	-	-	-	-	-	-	-

Electrode /Variable	k_1 (mol cm⁻² s⁻¹)	k_2 (mol cm⁻² s⁻¹)	a (V)	b (V)	θ	$\dfrac{Li^+}{Li^0}$	β (mol cm⁻²)	Q_{dl} (F cm⁻² s¹⁻ⁿ)	n_{dl}	σ (mol cm² s⁻¹/²)	R_e (Ω cm²)	R_{film} (Ω cm²)	Q_{film} (F cm⁻² s¹⁻ⁿ)	n_{film}
2	9.70×10^{-5}	4.27×10^{-6}	19	19	0.71	0.88	1.01×10^{-10}	4.59×10^{-3}	0.86	0	40	28.15	9.97×10^{-6}	0.98
3	8.18×10^{-5}	7.59×10^{-6}	19	18	0.79	0.73	9.99×10^{-7}	4.14×10^{-3}	0.85	0	31	146.93	1.00×10^{-5}	1
4	9.52×10^{-5}	6.38×10^{-6}	20	19	0.83	1.16	9.99×10^{-7}	6.41×10^{-3}	0.70	1279.76	40	602.47	1×10^{-5}	1
5	9.52×10^{-5}	6.46×10^{-6}	19	16	0.9	0.92	9.99×10^{-7}	8.48×10^{-3}	0.70	1998.34	37	216.3	1×10^{-5}	1
6	9.23×10^{-6}	4.49×10^{-6}	19	18	1	0.78	2.35×10^{-9}	1.60×10^{-5}	0.73	0	42	3030.80	9.90×10^{-5}	0.78

Table 3. Fitting results of the proposed model at 1.2V of bias potential.

Electrode /Variable	R_{film} (Ω cm²)	Q_{film} (F cm⁻² s¹⁻ⁿ)	n_{film}	R_{ct} (Ω cm²)	Q_{dl} (F cm⁻² s¹⁻ⁿ)	n_{dl}	R_e (Ω cm²)	-	-	-	-	-	-	-
1	71.79	1.53×10^{-4}	0.7	1424	6.70×10^{-3}	0.89	32.94	-	-	-	-	-	-	-

Electrode /Variable	k_1 (mol cm⁻² s⁻¹)	k_2 (mol cm⁻² s⁻¹)	a (V)	b (V)	θ	$\dfrac{Li^+}{Li^0}$	β (mol cm⁻²)	Q_{dl} (F cm⁻² s¹⁻ⁿ)	n_{dl}	σ (mol cm² s⁻¹/²)	R_e (Ω cm²)	R_{film} (Ω cm²)	Q_{film} (F cm⁻² s¹⁻ⁿ)	n_{film}
2	8.22×10^{-3}	5.70×10^{-5}	16	17	0.49	0.87	1.01×10^{-9}	4.56×10^{-3}	0.78	0	39	23.88	9.99×10^{-6}	1
3	2.38×10^{-3}	9.01×10^{-4}	17	19	0.54	0.73	9.99×10^{-7}	4.27×10^{-3}	0.80	0	20	137.14	8.52×10^{-6}	1
4	7.70×10^{-2}	3.72×10^{-4}	16	19	0.52	0.87	1.89×10^{-11}	1.77×10^{-3}	0.70	203.39	19	396.05	1×10^{-5}	1
5	1.57×10^{-2}	5.37×10^{-4}	18	19	0.57	0.50	4.73×10^{-11}	3.54×10^{-3}	0.70	312	22	300.14	1×10^{-5}	1
6	2.72×10^{-5}	2.45×10^{-5}	17	19	0.99	0.77	1.61×10^{-9}	7.05×10^{-5}	0.70	0	44	3687.88	9.69×10^{-5}	0.81

Table 4. Fitting results of the proposed model at 1.4V of bias potential.

Electrode /Variable	R_{film} (Ω cm^2)	Q_{film} (F cm^{-2} s^{1-n})	n_{film}	R_{ct} (Ω cm^2)	Q_{dl} (F cm^{-2} s^{1-n})	n_{dl}	R_e (Ω cm^2)
1	96.65	1.31×10^{-4}	0.76	370	5.62×10^{-3}	0.77	33.66
2	39.70	7.61×10^{-5}	0.80	335	5.39×10^{-3}	0.84	41.12
3	112.00	6.92×10^{-5}	0.81	470	3.35×10^{-3}	0.72	30.94
4	356.84	1.00×10^{-4}	0.74	748	3.46×10^{-3}	0.70	30.48
5	690.88	8.47×10^{-5}	0.76	1129	2.78×10^{-3}	0.74	32.18
6	2286.64	1.10×10^{-4}	0.70	6443	9.89×10^{-6}	0.7	82.40

Q_{dl} is the quantification of the energy used to align dipoles across Helmholtz double layer where the electrochemical reactions are taking place. Q_{dl} is very low (in the range 10^{-6} F cm^{-2} s^{1-n}) in the cathode with 100% LiMnPO$_4$ [20], which is the normal range for a surface with a negligible adsorption process. On the other hand, the Q_{dl} variable is higher in the electrode with 100% MWCNTs where a significant fraction of water molecules are absorbed (in the range 10^{-2} F cm^{-2} s^{1-n}) [20]. In the rest of the materials, the values of Q_{dl} are around the same magnitude due to the primary effect of adsorption at the MWCNTs. However, they change a little due to the activation of the particles of LiMnPO$_4$. The quantification of roughness/porosity of the electrode surface is reflected on the n_{dl} value, this quantity varies between 0.5 (porous electrodes) and 1 (ideal flat electrode) [46]. This geometry factor reflects the presence of particle aggregates in electrodes 4, 5, and 6, as shown in Fig. 2.

Q_{film} is the quantification of the energy used to align all of the dipoles of the composite film. This capacitance is the highest in electrode 1 when the salt water is the dominantte dielectric material ($\varepsilon_r \sim 50$) within the film [47]. In contrast, this value is very low at electrode 6 for all the conditions showing a low dielectric response of LiMnPO$_4$ ($\varepsilon_r \sim 8.1$) [48]. In the other electrodes, Q_{film} values are around 1×10^{-5} F cm^{-2} s^{1-n}, which reveals that the migration-diffusion in the electrolyte is associated with the presence of Li deintercalation. n_{film} can be qualitatively related to the roughness and porosity of the composite. We believe n_{film} is related to the relative same porosity; the change is negligible (Table 1).

The fitting results for 1.4 V are listed in Table 4. At this potential, the oxygen evolution reaction dominates the process on the electrodes. As the quantity of LiMnPO$_4$ increases in the electrode, R_{ct} as well as R_{film} increase. The pseudo-capacitances are on the order of magnitude of those of electrode 1, which did not experience deintercalation of lithium but the dielectric property of the electrolyte.

Intercalation factor (θ)

One of the most important variables is the intercalation factor, θ, listed in Tables 2–3. The intercalation factor changes a little at 0.8 V, a finding that is supported by the CV results. At 0.8, the intercalation factor was 0.71, 0.73, 0.83, 0.90, and 1.00 for electrodes 2, 3, 4, 5, and 6, respectively. Therefore, the addition of MWCNTs increases the conductivity of the particles, which results in faster current exchange for the Li extraction even at this potential. This finding is consistent with the results of previous studies done with the same model. The intercalation factor decreased with the addition of MWCNTs close to open circuit in a LiCoO$_2$ cathode [21], as shown in Fig. 6. The deintercalation factor decreases at 1.2 V as the percentage of MWCNTs increases. It was 0.49, 0.54, 0.52, 0.57, and 0.99 for electrodes 2, 3, 4, 5, and 6, respectively. These findings are in agreement with the oxidation peak acquired in the CV results (i.e., where the maximum current for the lithium deintercalation was approximately 1.2 V). The rate of deintercalation increased by several orders of magnitude, this is from 10^{-5} to 10^{-2} mol cm^{-2} s^{-1} with the potential increment. Therefore, the intercalation factor went down; the addition of MWCNTs helps to improve the performance of a LiMnPO$_4$ cathode but can also increase the charge transfer resistance due to higher adsorption and oxygen evolution as a side reaction. The effects of all the variables due to the potential modification are illustrated in Fig. 6.
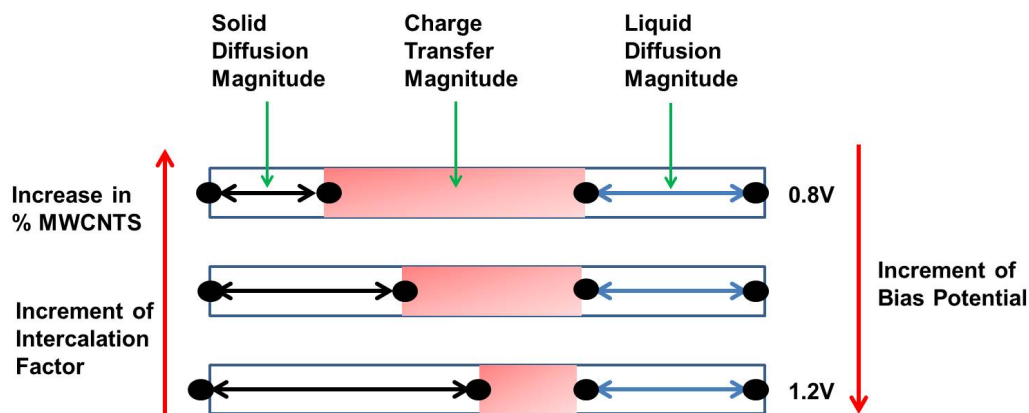
Fig. 6. Schematic illustration of the effect of several variables on the diffusion magnitudes and charge transfer resistance.

Conclusion

The SEM results revealed a porous surface with nearly the same percentage of porosity yielded a uniform liquid state diffusion rate. Cyclic voltammetry identified the redox potential of $LiMnPO_4$ and the onset of oxygen evolution. A capacitive behavior of the composite, the lithium deintercalation, and the water oxidation were noted between 0.8 and 1.4 V vs. Ag/AgCl. Electrochemical impedance spectroscopy showed the different behaviors of the electrode at 0.8, 1.2, and 1.4 V. At 0.8 V, the capacitive behavior of the porous structured electrode was the primary feature. However, as the fraction of $LiMnPO_4$ increased the intercalation process began to control the system at 60w%$LiMnPO_4$/40%MWCNTs and 80/20 ratios. At 1.2 V, the presence of a semicircle at LF was associated with the deintercalation of lithium and the water oxidation for electrodes 1, 2, and 3. In addition to electrodes 4 and 5, the semicircle at HF and MF was mainly related to the intercalation; the line at LF was related to the diffusion in the solid state in the $LiMnPO_4$. At 1.4 V, all of the behaviors in the EIS results were dominated by oxygen evolution. These dominating processes at each potential were demonstrated to correlate with the results of the coverage factor adapted to the lithium intercalation phenomena, which include the intercalation factor, the reaction kinetic constants, and the double layer capacitance.

Acknowledgment

References

1. Alias, N.; Mohamad, A. A. *J. Power Sources* **2015,** *274* (Supplement C), 237-251.
2. Wang, G. J.; Zhao, N. H.; Yang, L. C.; Wu, Y. P.; Wu, H. Q.; Holze, R. *Electrochim. Acta* **2007,** *52* (15), 4911-4915.
3. Broussely, M.; Planchat, J. P.; Rigobert, G.; Virey, D.; Sarre, G. *J. Power Sources* **1997,** *68* (1), 8-12.
4. Kim, H.; Hong, J.; Park, K. Y.; Kim, H.; Kim, S. W.; Kang, K. *Chem. Rev.* **2014,** *114* (23), 11788-11827.

5. Castaneda, H.; Tan, B.; Saunders, J. *Electrochim. Acta* **2010,** *55* (13), 4137-4143.
6. Köhler, J.; Makihara, H.; Uegaito, H.; Inoue, H.; Toki, M. *Electrochim. Acta* **2000,** *46* (1), 59-65.
7. Wang, Y.; Yi, J.; Xia, Y. *Adv. Energy Mater.* **2012,** *2* (7), 830-840.
8. Luo, J. Y.; Cui, W. J.; He, P.; Xia, Y. Y. *Nat. Chem.* **2010,** *2* (9), 760-765.
9. Wainwright, D. D., R. *Mat. Tech.* **1996,** *11*, 9-12.
10. Wang, Y.-g.; Luo, J.-y.; Wang, C.-x.; Xia, Y.-y. *J. Electrochem. Soc.* **2006,** *153* (8), A1425-A1431.
11. Yan, J.; Wang, J.; Liu, H.; Bakenov, Z.; Gosselink, D.; Chen, P. *J. Power Sources* **2012,** *216*, 222-226.
12. Padhi, A. K.; Nanjundaswamy, K. S.; Masquelier, C.; Okada, S.; Goodenough, J. B. *J. Electrochem. Soc.* **1997,** *144* (5), 1609-1613.
13. Yuan, L.-X.; Wang, Z.-H.; Zhang, W.-X.; Hu, X.-L.; Chen, J.-T.; Huang, Y.-H.; Goodenough, J. B. *Energy Environ. Sci.* **2011,** *4* (2), 269-284.
14. Xu, J.; Dou, S.; Liu, H.; Dai, L. *Nano Energy* **2013,** *2* (4), 439-442.
15. Doan, T. N. L.; Taniguchi, I. *J. Power Sources* **2011,** *196* (3), 1399-1408.
16. Aravindan, V.; Gnanaraj, J.; Lee, Y.-S.; Madhavi, S. *J. Mater. Chem. A* **2013,** *1* (11), 3518-3539.
17. Yonemura, M.; Yamada, A.; Takei, Y.; Sonoyama, N.; Kanno, R. *J. Electrochem. Soc.* **2004,** *151* (9), A1352-A1356.
18. Barpanda, P.; Djellab, K.; Recham, N.; Armand, M.; Tarascon, J.-M. *J. Mater. Chem.* **2011,** *21* (27), 10143-10152.
19. Rangappa, D.; Sone, K.; Zhou, Y.; Kudo, T.; Honma, I. *J. Mater. Chem.* **2011,** *21* (39), 15813-15818.
20. Chiu, T.-M.; Barraza-Fierro, J. I.; Castaneda, H. *Electrochim. Acta* **2017,** *253*, 93-103.
21. Rosas, O.; Saunders, J.; Castaneda, H. *Electrochim. Acta* **2013,** *113*, 77-86.
22. M. D. Levi, G. Salitra, B. Markovsky, H. Teller,a D. Aurbach, Udo Heider,b and Lilia Heider *J. Electrochem. Soc.* **1999,** *146*, 1279-1289.
23. Gauthier, M.; Carney, T. J.; Grimaud, A.; Giordano, L.; Pour, N.; Chang, H.-H.; Fenning, D. P.; Lux, S. F.; Paschos, O.; Bauer, C.; Maglia, F.; Lupart, S.; Lamp, P.; Shao-Horn, Y. *J. Phys. Chem. Lett.* **2015,** *6* (22), 4653-4672.
24. Jung, Y. S.; Cavanagh, A. S.; Dillon, A. C.; Groner, M. D.; George, S. M.; Lee, S. H. *J. Electrochem. Soc.* **2010,** *157* (1), A75-A81.
25. Macdonald, D. D. *Electrochim. Acta* **2006,** *51* (8–9), 1376-1388.
26. Macdonald, D. D. *Electrochim. Acta* **1990,** *35* (10), 1509-1525.
27. Chen, Z.; Wang, L. Y.; Yin, G.; Lin, F.; Wang, C. *IEEE Trans. on Energy Convers.* **2013,** *28* (4), 860-870.
28. Song, J.; Bazant, M. Z. *Phys. Rev. Lett.* **2018,** *120* (11).
29. Bai, L.; Conway, B. E. *Electrochim. Acta* **1993,** *38* (14), 1803-1815.
30. Epelboin, I.; Keddam, M.; Lestrade, J. C. *Faraday Discuss. Chem. Soc.* **1973,** *56* (0), 264-275.
31. Hernandez-Maya, R.; Rosas, O.; Saunders, J.; Castaneda, H. *J. Electrochem. Soc.* **2015,** *162* (4), A687-A696.
32. Schneider, C. A.; Rasband, W. S.; Eliceiri, K. W. *Nat. Meth.* **2012,** *9* (7), 671-675.
33. Hjelm, A.-K.; Lindbergh, G. *Electrochim. Acta* **2002,** *47* (11), 1747-1759.
34. Levi, M. D.; Salitra, G.; Markovsky, B.; Teller, H.; Aurbach, D.; Heider, U.; Heider, L. *J. Electrochem. Soc.* **1999,** *146* (4), 1279-1289.
35. Barraza-Fierro, J. I.; Campillo-Illanes, B.; Li, X.; Castaneda, H. *Metall. Mater. Trans. A* **2014,** *45* (9), 3981-3994.
36. Ahmad, A. L.; Ideris, N.; Ooi, B. S.; Low, S. C.; Ismail, A. *J. Appl. Sci.* **2014,** *14* (12), 1299-1303.
37. Li, G.; Azuma, H.; Tohda, M. *Electrochem. Solid-State Lett.* **2002,** *5* (6), A135-A137.
38. Oh, S.-M.; Oh, S.-W.; Yoon, C.-S.; Scrosati, B.; Amine, K.; Sun, Y.-K. *Adv. Funct. Mater.* **2010,** *20* (19), 3260-3265.
39. Kwon, N.-H.; Drezen, T.; Exnar, I.; Teerlinck, I.; Isono, M.; Graetzel, M. *Electrochem. Solid-State Lett.* **2006,** *9* (6), A277-A280.
40. Levi, M. D.; Aurbach, D. *J. Phys. Chem. B* **1997,** *101* (23), 4630-4640.
41. Cheng, M.-Y.; Ye, Y.-S.; Chiu, T.-M.; Pan, C.-J.; Hwang, B.-J. *J. Power Sources* **2014,** *253*, 27-34.

42. Huang, J.; Li, Z.; Zhang, J.; Song, S.; Lou, Z.; Wu, N. *J. Electrochem. Soc.* **2015,** *162* (4), A585-A595.
43. Manjunatha, H.; Venkatesha, T. V.; Suresh, G. S. *J. Solid-State Electrochem.* **2012,** *16* (5), 1941-1952.
44. Sinha, N. N.; Ragupathy, P.; Vasan, H. N.; Munichandraiah, N. *Int. J. Electrochem. Sci.* **2008,** *3*, 691-710.
45. Taylor, M. L. *Technological aspects of corrosion control in metallic systems.* The Pennsylvania State University, 2012.
46. Rammelt, U.; Reinhard, G. *Electrochim. Acta* **1990,** *35* (6), 1045-1049.
47. Hasted, J. B.; Ritson, D. M.; Collie, C. H. *J. Chem. Phys.* **1948,** *16* (1), 1-21.
48. Hu, X.; Cheng, Z.; Li, Y.; Ling, Z. *J. Alloys Compd.* **2015,** *651*, 290-293.